Catalytic molten metals for the direct conversion of methane to hydrogen and separable carbon

Authors: D. Chester Upham[1], Vishal Agarwal[1,2], Alexander Khechfe[3], Zachary R. Snodgrass[3], Michael J. Gordon[3], Horia Metiu[1*], Eric W. McFarland[3*]

Affiliations

[1]Department of Chemistry and Biochemistry, University of California, Santa Barbara, CA 93106-9510, USA.

[2]Department of Chemical Engineering, Indian Institute of Technology, Kanpur 208016, Uttar Pradesh, India.

[3]Department of Chemical Engineering, University of California, Santa Barbara, CA 93106-5080, USA.

*Correspondence to: metiu@chem.ucsb.edu, ewmcfar@engineering.ucsb.edu

Abstract:

Metals that are active catalysts for methane (Ni, Pt, Pd), when dissolved in inactive low melting temperature metals (In, Ga, Sn, Pb), produce stable molten metal alloy catalysts for pyrolysis of methane into hydrogen and carbon. All solid catalysts previously used for this reaction have been deactivated by carbon deposition. In the molten alloy system, the insoluble carbon floats to the surface where it can be skimmed off. A 27%Ni - 73%Bi alloy achieved 95% methane conversion at 1065°C in a 1.1-meter bubble column and produced pure hydrogen without CO_2 or other byproducts. Calculations show that the active metals in the molten alloys are atomically dispersed and negatively charged. There is a correlation between the amount of charge on the atoms and their catalytic activity.

One Sentence Summary:

Several molten metal alloys are stable catalysts for methane pyrolysis without being deactivated by carbon.

Main Text:

Hydrogen is an important chemical intermediate and could be used as a CO_2-free energy carrier in many applications that currently rely on fossil hydrocarbons. Steam methane (CH_4) reforming (SMR) followed by the water-gas shift reaction is the most common process for large-scale hydrogen production today (*1*). Although commercially optimized for decades, the endothermic SMR process is expensive; high capital costs and high energy consumption are unavoidable (*2*). In addition, the process produces stoichiometric CO_2, which may impose additional costs because of the need for sequestration or because of a possible carbon tax. Despite the fundamental process economic and environmental limitations of SMR, none of the

presently deployed renewable power sources, including hydrogen from electrolysis, can compete with the SMR process for large-scale H_2 production (*3*).

Alternatively, H_2 can be produced by pyrolysis of CH_4 without producing CO_2:

$$CH_4(g) \rightarrow C(s) + 2\ H_2(g) \qquad \Delta H^o = 74\ kJ/mole \qquad (1)$$

Only half as much H_2 is produced per mole of CH_4 compared to SMR; however, significantly less energy input is required and solid carbon is co-produced rather than CO_2. The solid carbon can be safely stored in perpetuity; some may be valuable for use in electrodes or as additives to materials (e.g. concrete, asphalt, rubber). Further, direct CH_4 pyrolysis can be done in a relatively simple (and potentially low-cost) commercial process in a single reaction step. Small amounts of unconverted CH_4 can be tolerated in most downstream processes. For ammonia production or in a fuel cell, for example, H_2 may contain small amounts of CH_4, whereas carbon oxides produced from the SMR process will poison the catalysts and must be completely removed.

Early interest in CH_4 pyrolysis made use of gas-phase radical reactions. Reaction equilibrium favors high temperature and low pressure to achieve high CH_4 conversion, and high-temperature gas phase chemistry co-produces a mixture of H_2 along with ethane, ethylene, acetylene, and aromatics, which are expensive to separate (*4*). The only commercially practiced processes use gas-phase reactions in thermochemical or plasma reactor systems (*5*) to produce specialty carbons; however, CH_4 pyrolysis has not been used commercially specifically for H_2 production. Reports by Steinberg (*6*) and others (*7-15*) have proposed using inert molten metals as a thermochemical reaction media and as a heat transfer fluid for pyrolysis of CH_4. In molten metals, the low-density carbon produced by gas-phase pyrolysis at high temperature floats to the surface of the melt where it can be removed. The highest H_2 yield of 78% at 1175°C was obtained in a 1-meter bubble column containing molten tin, which is not thought to be catalytic (*15*). Technoeconomic analyses using several heating strategies show that H_2 can potentially be produced by pyrolysis at approximately the same cost as that of SMR (*6*), and that using a catalytically active and selective molten metal catalyst producing continuously separable carbon could make the cost of H_2 competitive with SMR even without a CO_2 tax (*16*).

Metallic catalysts (e.g. Ni, Pd, Pt) achieve high conversion and selectivity to H_2 at moderate temperatures; however, their melting temperatures are extremely high and as solids are rapidly deactivated by solid carbon (coke) (*6, 8, 17-19*). The only report of the use of a molten metal as a catalyst for CH_4 pyrolysis described pure liquid magnesium (Mg), which was used to achieve ~30% of the equilibrium conversion, at 700°C (*20*). Higher conversions, at higher temperatures, were not possible because of Mg evaporation.

We prepared liquid alloys of active metals in low-melting-temperature metal "solvents" (Sn, Pb, Bi, In, and Ga) using known equilibrium phase behavior to produce catalysts that melt at < 1000°C, and examined the catalytic properties of such melts. We used density function theory to explore physical properties of atoms and clusters of atoms introduced into melts as they relate to the catalytic activity of the melt. The melts are used in molten-metal bubble columns, where carbon continuously floats to the surface where it can be removed (Figure 1).

A differential reactor (Fig S1A (*21*)) was used to compare the specific activities for CH_4 pyrolysis for 21 metals and alloys (Table 1). Four trends are notable. First, low-melting-temperature metal "solvents" had some activity, in the order In < Bi < Sn < Ga < Pb. Second, the addition of an active component increased the reaction rate and the magnitude of this increase depends on the solvent metal used. For example, the activity of melts containing 17 mole % of Ni increased as the solvent changed, the order being In < Sn < Ga < Pb < Bi. Third, the activity increased with the amount of the active metal; for example, 73 mole % of Ni in In was more active than 17 mole % of Ni in In. Fourth, Ni was always more active than Pt, for the same solvent, whereas solid Pt and solid Ni have approximately the same activity (*18*). Of the compositions we tested, 27 mole % of Ni dissolved in molten Bi ($Ni_{0.27}Bi_{0.73}$) was the most active catalyst we found, and further experimental work focused on this alloy.

An effective activation energy E_a of 208 kJ/mole was determined for the $Ni_{0.27}Bi_{0.73}$ melt from the data in the Arrhenius plot shown in Fig. 2A obtained in a 15-cm bubble column (Fig. 2B). This value is lower than the activation energy for CH_4 pyrolysis in Bi liquid or for the uncatalyzed gas-phase reaction, but it is higher than that for carbon or solid Ni catalysts (see Fig. 2B). This difference indicates that Ni dissolved in Bi is different from Ni solid, and that $Ni_{0.27}Bi_{0.73}$ is different from Bi solid, or a physical mixture of Ni and Bi.

We observed 95% CH_4 conversion in a 1.1-m bubble column containing molten $Ni_{0.27}Bi_{0.73}$ (Fig. 3A) at 1065°C. Under these reaction conditions, the equilibrium conversion is 98%. When the temperature was reduced to 1040°C, the CH_4 conversion decreased to 86%. The effect of residence time was measured by adjusting the depth at which gas was introduced in the 1.1-meter bubble column (see Fig. S1C (*21*)). The temperature in the top 5 cm of the bubble column was maintained cooler by ~100°C, to minimize reactions in the gas headspace above the melt. Procedures and concerns related to the safe operation of molten-metal bubble columns are addressed in the supplemental information.

Kinetic data obtained in a differential bubble column reactor were used to model a large-scale reactor. The rate expression was determined using the activation energy from the Arrhenius plot (Fig. 2A), and the first-order pressure dependence was determined in a separate experiment (Fig. 3B and 3C). The conversion as a function of the surface area was then calculated at 1040°C and plotted with the experimental data (Fig. 3A). At 1065°C, in the 1.1-m bubble rise column, only H_2 was observed in the product effluent; no byproducts were detectable. In a separate experiment, propane was also observed to completely decompose to hydrogen and carbon at 1000°C in a 12-cm column. Higher pressures resulted in less selectivity to hydrogen (Fig 3C) in a differential reactor, which may be due to gas-phase reactions occurring; however at longer residence times, the lack of byproducts suggest that any other products pyrolyze at least as rapidly as methane. The CH_4 data were used to make an estimate of approximately 600 m^3 for the reactor required for a 200 kilotons per annum H_2 plant, operating at 10 atm, with 95% CH_4 conversion at 1065°C, assuming 25% gas-phase hold up, continuous carbon removal, and approximately spherical, 1-cm diameter, bubbles (see supplementary information).

The stability of $Ni_{0.27}Bi_{0.73}$ as a catalyst for CH_4 pyrolysis was determined by measuring pyrolysis activity over time. The activity of a bubble column of molten $Ni_{0.27}Bi_{0.73}$ did not change over 170 hours (Fig. S2 (*21*)). Over this time period, carbon dissolved into the melt and approached a steady state with the rate of precipitation out of the melt. A solid nickel catalyst deactivated in 1 hour (Fig. S3 (*21*)), likely forming a carbon-covered surface.

The carbon produced by CH_4 pyrolysis in a $Ni_{0.27}Bi_{0.73}$ bubble column accumulated as a fine powder at the top surface of the melt (Fig. 1, A and B). Raman spectroscopy indicated that most of the carbon was graphite (0.594 I(D)/I(G), Fig. 1C). A sharp peak at 284.5 eV in XPS (Fig. S4 (*21*)) also suggested that most of the carbon was graphitic. Energy-dispersive x-ray spectroscopy (EDX) showed that the powder was mostly carbon (92% of atoms) with small amount of Bi and Ni (total <4% of atoms) (Fig. S6 (*21*)). The metal was deposited by evaporation from the liquid and deposition on the floating carbon layer (Fig. S7 (*21*)). If the carbon layer was submerged in the melt, the Ni and Bi dissolved and clean carbon floated on the surface, where it could be removed (Fig. S8 (*21*)). Carbon also deposited slowly on the walls of the reactor via precipitation from the saturated melt; carbon was observed on walls that were never in contact with the CH_4 bubbles (Fig. S5 (*21*)). The rate of deposition on the reactor walls depended initially on the reactor material. However, once carbon formed, the carbon-on-carbon deposition decreased with time.

X-ray fluorescence measurements of cooled $Ni_{0.27}Bi_{0.73}$ alloy, after 170 hours of methane pyrolysis, showed that 1.5 mole % carbon has dissolved in the melt. Based on an assumed saturation of 1.5 atom % carbon, the time required to reach saturation in a bubble column is 5 hours; however, CH_4 conversion was constant through the time of saturation (Figs. S2, S3 (*21*)), indicating that the catalytic activity was not affected by the concentration of carbon on the melt. Constant conversion would be consistent with the cleavage of the C-H bond being the rate-limiting step.

To explore the behavior of carbon in the melt, a U-shaped reactor (Fig. S1B (*21*)) was filled with $Ni_{0.27}Bi_{0.73}$, and CH_4 bubbles were introduced in one arm of the U tube and Ar bubbles in the other. The gas streams were isolated from each other with no gas contact. After 7 days of continuous operation at 1050°C, most of the carbon formed accumulated above the surfaces of the melt -- on both sides of the tube. This observation is consistent with carbon formation from CH_4 pyrolysis at the surfaces of the CH_4-containing bubbles, saturating the metal alloy liquid with carbon such that precipitation occurs at all heterogeneous interfaces (including the surfaces of both CH_4 and Ar bubbles).

Constant-temperature ab initio molecular dynamics was used to investigate the electronic properties of the molten alloys. Initial calculations were performed for a melt containing one active metal atom in 82 atoms of inert material. In all cases, the active metal atom becomes negatively charged. Fig. 1C shows that, for Pt in Sn, the negative charge occupies an orbital whose shape is similar to that of a d-orbital. Because the system is liquid, the shape of the orbital and its energy fluctuate (Movie S1 (*21*)). The Bader charges of the active atoms in several melts are shown in Table S1 (*21*). Fig. 4A shows that the calculated charge on the active atom is correlated with the catalytic activity measured experimentally for CH_4 pyrolysis: the lesser the negative charge, the higher the activity. The electron charge on the active metal comes

from the neighboring Sn atoms, each having a slightly more positive Bader charge than when they are alone in the melt (Fig. 4B and 4C). The average charge per atom is –0.91 electron and no Pt-Pt bonds are formed. In retrospect, this finding is not surprising: Pt is an electrophilic metal and barium and cesium platinides are known compounds in which Pt is a negative ion (*22, 23*). The addition of Bi to Pt-group metals has also been observed to weaken the binding strength of aromatic hydrocarbons to the surface (*24*).

In simulations, we followed the evolution of Pt_2 (Fig. 4D and Movie S2 (*21*)) and Pt_8 clusters (Fig. S10 (*21*)) placed in molten Sn at 627°C. Both clusters dissociate in a few picoseconds to form isolated Pt^{-1} ions. This result is surprising for several reasons. Hybrid density functional calculations using the HSE06 functional show that Pt_2, Pt_2^{2-}, and even Pt_2^{4-} are stable in the gas phase and have a binding energy □0.5 eV. None would dissociate spontaneously in the gas. Further, dissociation of a molecule in a liquid is normally hindered by a "cage effect": the dissociation fragments need to have enough energy to push the solvent out of the way. Thus, Pt-cluster dissociation should be an activated process occurring on a time scale longer than a nanosecond. The only explanation for the rapidity of the dissociation is that electrons from Sn move rapidly to fill antibonding orbitals in Pt, which weakens the Pt-Pt bonds and charges the Pt atoms negatively, causing a "Coulomb explosion."

Based on ab initio molecular dynamics calculations, the nickel within the melt is atomic with a partial negative charge. The atomic charge in different alloys correlates to catalytic activity for CH_4 pyrolysis. If we can assume that the active site for methane activation is the dissolved active metal, the melts discussed here are "single atom" catalysts.

Supplementary content: Materials and Methods; Supplementary Text; Figures S1 to S12; Table S1; Movies S1 and S2 and captions; References *(29-43)*

References and Notes:

1. A. Bakenne, W. Nuttall, N. Kazantzis, Sankey-Diagram-based insights into the hydrogen economy of today. *Int. J. Hydrogen Energy* ***41***, 7744-7753 (2016).
2. C. H. Bartholomew, R. J. Farrauto, *Fundamentals of Industrial Catalytic Processes* (Wiley, 2011).
3. P. Nikolaidis, A. Poullikkas, A comparative overview of hydrogen production processes. *Renewable Sustainable Energy Rev.* ***67***, 597-611 (2017).
4. G. P. Van Der Zwet, P. A. J. M. Hendriks, R. A. Van Santen, Pyrolysis of methane and the role of surface area. *Catal. Today* ***4***, 365-369 (1989).
5. J. R. Fincke, R. P. Anderson, T. Hyde, B. A. Detering, R. Wright, R. L. Bewley, D. C. Haggard, W. D. Swank, Plasma thermal conversion of methane to acetylene. *Plasma Chem. Plasma Process.* ***22***, 105-136 (2002).
6. M. Steinberg, Fossil fuel decarbonization technology for mitigating global warming. *Int. J. Hydrogen Energy* ***24***, 771-777 (1999).
7. M. Serban, M. A. Lewis, C. L. Marshall, R. D. Doctor, Hydrogen production by direct contact pyrolysis of natural gas. *Energy Fuels* ***17***, 705-713 (2003).

8. A. Abánades, E. Ruiz, E. M. Ferruelo, F. Hernández, A. Cabanillas, J. M. Martínez-Val, J. A. Rubio, C. López, R. Gavela, G. Barrera, C. Rubbia, D. Salmieri, E. Rodilla, D. Gutiérrez, Experimental analysis of direct thermal methane cracking. *Int. J. Hydrogen Energy* ***36***, 12877-12886 (2011).
9. A. Abánades, C. Rubbia, D. Salmieri, Technological challenges for industrial development of hydrogen production based on methane cracking. *Energy* ***46***, 359-363 (2012).
10. D. Paxman, S. Trottier, M. Nikoo, M. Secanell, G. Ordorica-Garcia, Initial experimental and theoretical investigation of solar molten media methane cracking for hydrogen production. *Energy Procedia* ***49***, 2027-2036 (2014).
11. M. Plevan, T. Geissler, A. Abánades, K. Mehravaran, R. K. Rathnam, C. Rubbia, D. Salmieri, L. Stoppel, S. Stückrad, T. Wetzel, Thermal cracking of methane in a liquid metal bubble column reactor: Experiments and kinetic analysis. *Int. J. Hydrogen Energy* ***40***, 8020-8033 (2015).
12. T. Geissler, M. Plevan, A. Abanades, A. Heinzel, K. Mehravaran, R. K. Rathnam, C. Rubbia, D. Salmieri, L. Stoppel, S. Stuckrad, A. Weisenburger, H. Wenninger, T. Wetzel, Experimental investigation and thermo-chemical modeling of methane pyrolysis in a liquid metal bubble column reactor with a packed bed. *Int. J. Hydrogen Energy* ***40***, 14134-14146 (2015).
13. I. Schultz, D. W. Agar, Decarbonisation of fossil energy via methane pyrolysis using two reactor concepts: Fluid wall flow reactor and molten metal capillary reactor. *Int. J. Hydrogen Energy* ***40***, 11422-11427 (2015).
14. A. Abánades, R. K. Rathnam, T. Geissler, A. Heinzel, K. Mehravaran, G. Müller, M. Plevan, C. Rubbia, D. Salmieri, L. Stoppel, S. Stückrad, A. Weisenburger, H. Wenninger, T. Wetzel, Development of methane decarbonisation based on liquid metal technology for CO_2-free production of hydrogen. *Int. J. Hydrogen Energy* ***41***, 8159-8167 (2016).
15. T. Geissler, A. Abánades, A. Heinzel, K. Mehravaran, G. Müller, R. K. Rathnam, C. Rubbia, D. Salmieri, L. Stoppel, S. Stückrad, A. Weisenburger, H. Wenninger, T. Wetzel, Hydrogen production via methane pyrolysis in a liquid metal bubble column reactor with a packed bed. *Chem. Eng. J.* ***299***, 192-200 (2016).
16. B. Parkinson, J. W. Matthews, T. B. McConnaughy, D. C. Upham, E. W. McFarland, Techno-economic analysis of methane pyrolysis in molten metals: Decarbonizing natural gas. *Chem. Eng. Technol.* ***40***, 1022-1030 (2017).
17. N. Z. Muradov, How to produce hydrogen from fossil-fuels without CO_2 emission. *Int. J. Hydrogen Energy* ***18***, 211-215 (1993).
18. T. V. Choudhary, E. Aksoylu, D. W. Goodman, Nonoxidative activation of methane. *Catalysis Reviews* ***45***, 151-203 (2003).
19. H. F. Abbas, W. Daud, Hydrogen production by methane decomposition: A review. *Int. J. Hydrogen Energy* ***35***, 1160-1190 (2010).
20. K. Wang, W. S. Li, X. P. Zhou, Hydrogen generation by direct decomposition of hydrocarbons over molten magnesium. *J. Mol. Catal. A: Chem.* ***283***, 153-157 (2008).
21. Figures S1-S12, Movies S1 and S2, and details of experiments and calculations are available as supplementary materials.
22. A. Karpov, J. Nuss, U. Wedig, M. Jansen, Cs_2Pt: A platinide(-II) exhibiting complete charge separation. *Angew. Chem. Int. Ed.* ***42***, 4818-4821 (2003).

23. A. Karpov, M. Konuma, M. Jansen, An experimental proof for negative oxidation states of platinum: ESCA-measurements on barium platinides. *Chem. Commun.* ***2006***, 838-840 (2006).
24. C. T. Campbell, Bismuth Postdosing Thermal Desorption Mass Spectrometry (BPTDS). *Critical Reviews in Surface Chemistry* ***4***, 49-75 (1994).
25. T. Keipi, K. E. S. Tolvanen, H. Tolvanen, J. Konttinen, Thermo-catalytic decomposition of methane: The effect of reaction parameters on process design and the utilization possibilities of the produced carbon. *Energy Convers. Manage.* ***126***, 923-934 (2016).
26. H. B. Palmer, T. J. Hirt, The activation energy for the pyrolysis of methane. *J. Phys. Chem.* ***67***, 709-711 (1963).
27. N. Muradov, F. Smith, A. T-Raissi, Catalytic activity of carbons for methane decomposition reaction. *Catal. Today* ***102–103***, 225-233 (2005).
28. N. Muradov, Catalysis of methane decomposition over elemental carbon. *Catal. Commun.* ***2***, 89-94 (2001).
29. G. Kresse, J. Hafner, Ab-initio molecular-dynamics for liquid-metals. *Phys. Rev. B* ***47***, 558-561 (1993).
30. G. Kresse, J. Hafner, Ab-Initio molecular-dynamics simulation of the liquid-metal amorphous-semiconductor transition in germanium. *Phys. Rev. B* ***49***, 14251-14269 (1994).
31. G. Kresse, J. Furthmüller, Efficient iterative schemes for ab initio total-energy calculations using a plane-wave basis set. *Phys. Rev. B* ***54***, 11169-11186 (1996).
32. G. Kresse, J. Furthmüller, Efficiency of ab-initio total energy calculations for metals and semiconductors using a plane-wave basis set. *Comput. Mater. Sci.* ***6***, 15-50 (1996).
33. J. P. Perdew, K. Burke, M. Ernzerhof, Generalized gradient approximation made simple. *Phys. Rev. Lett.* ***77***, 3865-3868 (1996).
34. P. E. Blöchl, Projector augmented-wave method. *Phys. Rev. B* ***50***, 17953-17979 (1994).
35. R. Bader, *Atoms in Molecules: A Quantum Theory* (Clarendon, Oxford, 1994).
36. G. Henkelman, A. Arnaldsson, H. Jonsson, A fast and robust algorithm for Bader decomposition of charge density. *Comput. Mater. Sci.* ***36***, 354-360 (2006).
37. S. Grimme, J. Antony, S. Ehrlich, H. Krieg, A consistent and accurate ab initio parametrization of density functional dispersion correction (DFT-D) for the 94 elements H-Pu. *J. Chem. Phys.* ***132***, 154104 (2010).
38. W. G. Hoover, Canonical dynamics: Equilibrium phase-space distributions. *Phys. Rev. A* ***31***, 1695-1697 (1985).
39. S. Nosé, A molecular dynamics method for simulations in the canonical ensemble. *Mol. Phys.* ***52***, 255-268 (1984).
40. S. Nosé, A unified formulation of the constant temperature molecular dynamics methods. *J. Chem. Phys.* ***81***, 511-519 (1984).
41. L. Verlet, Computer "experiments" on classical fluids. I. Thermodynamical properties of Lennard-Jones molecules. *Physical Review* ***159***, 98-103 (1967).
42. J. R. DiPalma, Bismuth toxicity, often mild, can result in severe poisonings. *Emergency Medicine News* ***23***, 16 (2001) http://journals.lww.com/em-news/Fulltext/2001/04000/Bismuth_Toxicity,_Often_Mild,_Can_Result_in_Severe.12.aspx
43. V. Agarwal, H. Metiu, Oxygen vacancy formation on α-MoO_3 slabs and ribbons. *J. Phys. Chem. C* ***120***, 19252-19264 (2016).

Acknowledgments: This work was primarily supported by the U.S. Department of Energy, Office of Science Basic Energy Sciences Grant number DE-FG03-89ER14048, with additional support provided through a Mellichamp Sustainability Fellowship to DCU from the Mellichamp Academic Initiative. Artwork in Figure 1 was done by Peter Allen and Brian Long from the UCSB College of Engineering. Additional support to AK was provided by the UCSB Material Research Laboratory's Research Internships in Science and Engineering program. We made use of Center for Scientific Computing at the California NanoSystems Institute funded in part by NSF CNS-0960316 and Hewlett-Packard. The MRL Shared Experimental Facilities are supported by the MRSEC Program of the NSF under Award No. DMR 1121053; a member of the NSF-funded Materials Research Facilities Network (www.mrfn.org). All data are reported in the main paper and supplement.

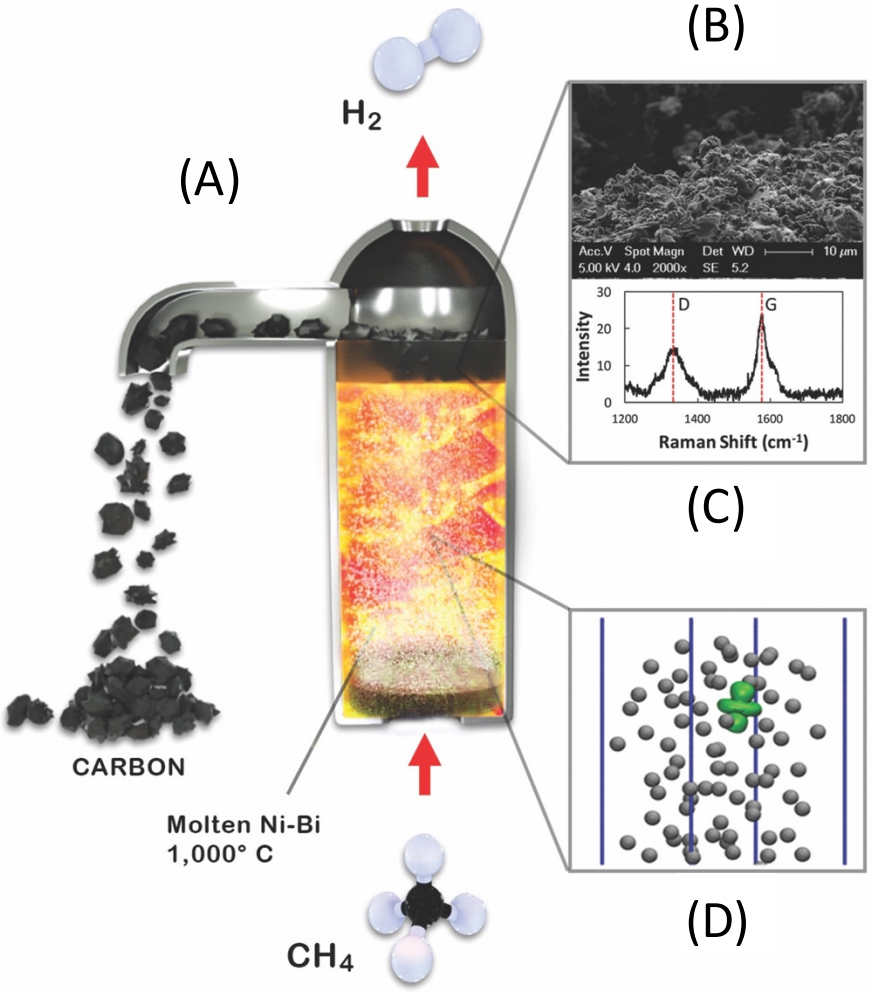

Fig. 1. Hydrogen production with a Ni-Bi molten catalyst. (A) Reactor for CH_4 conversion to H_2 and carbon in a molten-metal bubble column with continuous carbon removal. (B) Scanning electron microscopy (SEM) image of the carbon produced. (C) Raman spectrum of surface carbon. (D) Ab initio molecular dynamics simulation showing an orbital (green) of a Pt atom dissolved in molten Bi (grey) alloy.

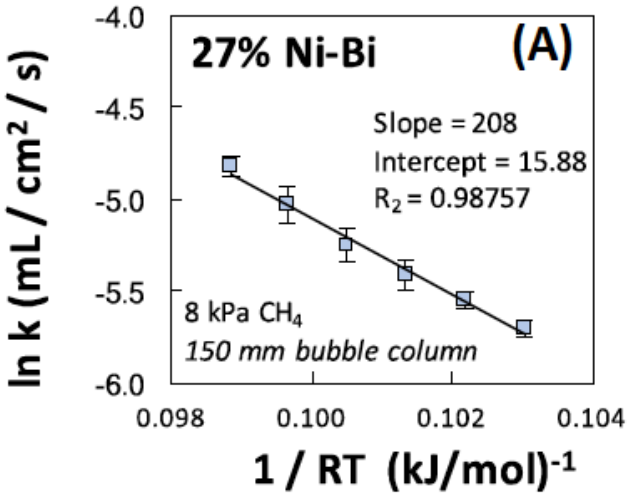

	(B) Catalyst	Activation Energy (kJ)
Separable	Ni-Bi liquid	208
	Bi liquid	310
	Gas-phase *(25)*	422
Non-separable	Ni *(26)*	65
	Activated C *(26)*	194
	Carbon black *(27)*	205-236
	Graphite, CNTs, nanotubes *(28)*	>carbon black

Fig. 2. Reaction kinetics. (A) Arrhenius plot for determination of apparent activation energy of Ni-Bi melt with 27 mole % Ni, in a differential reactor bubble column. (B) Apparent activation energies for metals, from this work and literature (*25-28*).

Table 1. Comparison of activity for methane pyrolysis at 1000°C when CH_4 is flowed over 38.5 mm^2 of molten metal as described in Figure S1A. The same reactor volume was used in all cases, including for Pb vapor. All compositions are molar percent. An asterisk (*) indicates that alloy is at the solubility limit of the dissolved active metal at 950°C.

Liquid catalyst	**Rate of hydrogen production (mol H_2 produced × cm^{-2} s^{-1})**
In	8.2×10^{-11}
Bi	8.2×10^{-11}
Sn	8.5×10^{-10}
Ga	3.2×10^{-9}
Pb	3.3×10^{-9}
Ag	4.3×10^{-9}
Pb vapor	2.1×10^{-9}
17% Cu-Sn*	3.1×10^{-9}
17% Pt-Sn	1.6×10^{-9}
17% Pt-Bi	4.2×10^{-9}
62% Pt-Bi*	6.5×10^{-9}
17% Ni-In	4.7×10^{-9}
17% Ni-Sn	5.6×10^{-9}
73% Ni-In*	6.4×10^{-9}
17% Ni-Ga	7.9×10^{-9}
17% Ni-Pb	8.3×10^{-9}
17% Ni-Bi	9.0×10^{-8}
27% Ni-Au*	1.2×10^{-8}
27% Ni-Bi*	1.7×10^{-8}
27% Ni-Bi* (replicate)*	1.7×10^{-8}

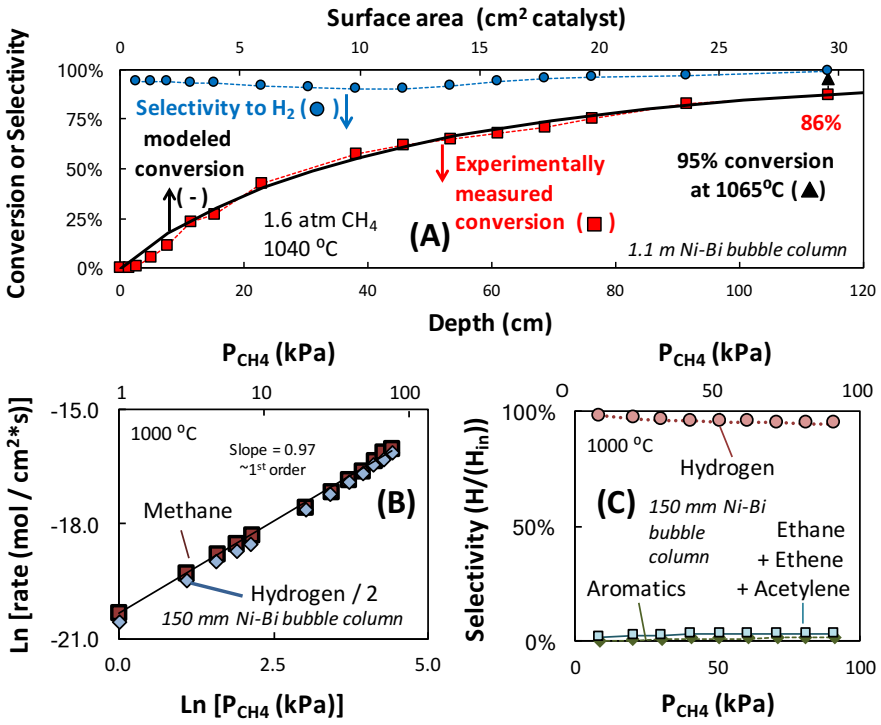

Fig. 3. Reactivity in a bubble column. (A) Experimentally observed methane conversion and selectivity to hydrogen as a function of inlet-tube depth and calculated bubble surface area for the reactor described in Figure S1c. The average temperature was 1040°C, except the top 5 cm, which was kept 100°C cooler to prevent headspace reactions. The black triangle represents data at 1065°C. 27 mole % Ni in Bi was used with a quartz inlet tube, at 160 kPa methane and 40 kPa argon inlet partial pressures, 10-standard centimeters per minute (sccm) total flow, and a 304 stainless-steel reactor. At 1065°C and 110 cm, hydrogen was the only product observed. (B) Logarithm of rate of CH_4 conversion and H_2 yield as a function of the logarithm of pressure. (C) Selectivity for pyrolysis at 1000°C as a function of CH_4 partial pressure in argon. The reactor for (B) and (C) was a 150-mm straight quartz differential bubble column.

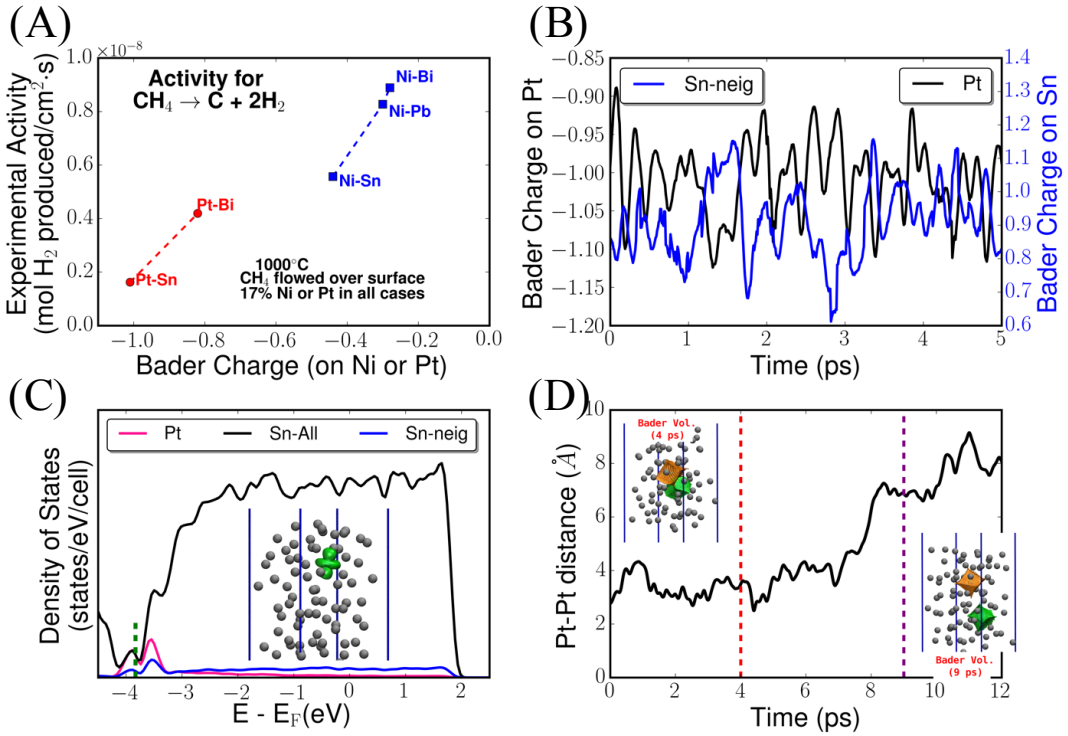

Fig 4. Theoretical results. (A) Activity for pyrolysis at 1000°C plotted versus calculated Bader charge on the active element. In all experiments, 17 mole percent platinum or nickel was used. The calculations used 1.2% mole Pt or Ni, at 627°C. (B) The time evolution of the Bader charge on a Pt atom dissolved in molten Sn, and the sum of Bader charges on nearest-neighboring Sn atoms during an AIMD run. (C) Projected density of states of a Pt atom, of the Sn atoms neighboring the Pt atom, and of all Sn atoms. The graph also shows, in green, the shape of one Pt orbital. The boundaries of simulation box are shown in blue. (D) The graph shows the distance between Pt atoms in a Pt_2 cluster in molten Sn during an AIMD run. The two pictures show the charges on the Pt atoms of a Pt_2 cluster at two different times.

Supplementary Materials for

Catalytic molten metals for the direct conversion of methane to hydrogen and separable carbon

D. Chester Upham, Vishal Agarwal, Alexander Khechfe, Zachary R. Snodgrass, Michael J. Gordon, Horia Metiu*, Eric W. McFarland*
*correspondence to: metiu@chem.ucsb.edu, ewmcfar@engineering.ucsb.edu

This PDF file includes:

Other Supplementary Materials for this manuscript includes the following:

Materials and Methods

Screening reactor

Liquid metal catalysts, having the same surface area, were compared in the reactor described in Fig. S1a. A quartz tube was used to hold a ceramic cap with 38.5-mm^2 surface area that was filled with metal and melted to reach the top of the cap. Powdered metals were mixed and melted. Metal oxides were reduced by flowing hydrogen at 1000°C until no hydrogen conversion was observed. All metals were purchased from Sigma Aldrich. A mixture of methane (0.25 sccm) and argon (2.25 sccm) was then flown over the surface using mass flow controllers (MKS 1179). A mass spectrometer (SRS RGA 200) was used to analyze the products. The hydrogen produced in a blank reactor was subtracted from the total hydrogen produced.

Lead has a high vapor pressure and vapor formation was observed. The activity of the vapor, without the liquid surface, was measured using the same reactor without any liquid in the ceramic cap. The lead vapor was introduced from a reservoir below the reactor but still in the furnace at 1000°C with 2.25 sccm argon carrying the vapor into the reactor where 0.25 sccm CH_4 was introduced.

When solid metals were tested, an empty reactor with an empty alumina crucible was used as described in Figure S1a. In order to use the same surface area as that of the liquid, the surface area per cm^2 was determined by the Brunauer-Emmett-Teller method (BET), and an appropriate length of wire to give the same surface area as the liquid metals was used. The wire was placed in the inner part of the tube introducing gas immediately above the alumina crucible.

The 150-mm quartz U-tube bubble column reactor

A bubble column with two separate inlets and outlets was constructed out of quartz and connected to a mass spectrometer to analyze the products (Fig. S1b). Gas was passed through each side of the U-tube, and bubbles floated to each surface of each arm, independently of each other. The molten metal reactor had 150 mm of liquid on each side, was 12 mm in diameter, and had a 3-mm quartz tube on each side that went down into the liquid metal to introduce the gases. The depth of the tube could be controlled to any height using Swagelok UltraTorr fittings. A 850-watt Watlow ceramic fiber heater was used to heat the entire liquid. A mass spectrometer (SRS RGA 200) was used to analyze the products of one side at a time. Mass flow controllers (MKS 1179) were used to deliver methane and argon through Teflon lines that were heated to 110°C in an oven. The temperature was controlled using a K-type thermocouple inside the furnace but outside the reactor tube. The region in which the molten metal was isothermal was determined by inserting a thermocouple inside the reaction gas inlet and measuring the temperature profile. The reactor was placed so that the head space had a lower temperature than the melt.

The 150-mm straight quartz bubble column reactor

A bubble column reactor was constructed out of quartz and connected to a mass spectrometer to analyze the products (straight version of Fig. S1b). The molten metal column was 150 mm high and 12 mm in diameter. A 3-mm quartz tube, which went down into the liquid

metal, was used to introduce gas into the melt. The heater, mass spectrometer, oven, and mass flow controllers were the same as those used in the U-tube.

The 1.1-m stainless steel bubble column reactor

A 304 stainless steel bubble column was used (Figure S1c) with the same flow control and product analysis as the 150-mm bubble column. The tube was 3 cm × 1.2 m and closed on one end with a welded cap. The reactor was fitted into a 4-cm alumina sleeve, which was surrounded by four 30.5-cm 850 Watt ceramic heaters (Watlow) surrounded by ceramic insulation. The space between the alumina tube and the stainless-steel reactor was slowly purged with nitrogen gas to prevent scaling of the stainless steel by oxidation at high temperatures. The bottom of the reactor and heaters were supported by ceramic insulation on a sand bed.

The temperature of each of the four heaters was controlled independently using thermocouples inside the furnace. A 6-mm 316 stainless steel tube with a closed end was inserted into the melt as a sleeve for a K-type thermocouple. The thermocouple inside the melt was used to adjust the temperature profile of the reactor to get as close to isothermal conditions as possible. A 3-mm quartz tube was used to introduce the gas and was inserted from the top of the reactor. In order to prevent reactions in the headspace, possibly catalyzed by the stainless steel, the top 5 cm of the melt was kept cool by filling the tube above the level of the heaters and cooling in air with a fan from the outside. Nickel and bismuth for this reactor were purchased from Rotometals.

Characterization techniques

The carbon powder from the top of the melt was characterized using Raman spectroscopy and X-ray photoelectron spectroscopy (XPS). A Horiba Jobin Yvon LabRAM Aramis was used to obtain Raman spectra. Fifteen Raman spectra were taken at different locations in the powder using a 633-nm laser, and the intensity ratio I(D)/I(G) was calculated for each, where I(D) is the intensity of the D peak (1350 cm^{-1}) and I(G) is the intensity of the G peak (1600 cm^{-1}). These intensity ratios were then averaged to obtain an overall degree of graphitization for the carbon. One representative spectra was reported in Fig. 1.

High resolution XPS scans of the carbon powder were performed on a Kratos Axis Ultra XPS system with a monochromated Al X-ray source. A step size of 50 meV and a dwell time of 200 ms were used with no charge neutralization. The pressure of the analytical chamber was kept below 5.0 × 10-8 torr during the analysis.

X-ray fluorescence (XRF) was used to quantify the amount of carbon left over in the melt post-cooling. To obtain quantitative data, standards containing 0, 2.5, 5, 10, 20, and 30 mol% C in the 30 mol% Ni-Bi alloy were prepared. These standards were prepared by milling a 30 mol% Ni-Bi alloy into a fine powder and adding the corresponding amount of graphite powder. The metal and graphite powders were then mixed with a mortar and pestle until homogeneous. The standard powders were pressed into 13 mm diameter wafers using a hydraulic press and die-kit. A wafer of material from the U-tube was created by milling and pressing in a similar fashion. A Rigaku ZSX Primus IV was used to carry out quantitative XRF measurements. A 10-mm beam was used with sample rotation to ensure high signal from the sample. No silicon signal was observed in XRF, which would be present if quartz had dissolved in the melt.

Computational details

The simulation cell used for the density functional calculations consists of a liquid film of 82 non-active metal atoms (either Sn, Bi, or Pb). We studied the effect of adding Ni, Pd, and Pt to this molten system. The area of the liquid surface is 12Å×12Å. The liquid surface fluctuates during the simulations and is in contact with vacuum. The height of the simulation box was obtained from benchmarking calculations so that a minimum vacuum thickness of 12 Å is obtained in all cases. The *ab initio*, constant temperature, molecular dynamics (AIMD) simulations were performed with the forces given by the density function theory (DFT) using the VASP simulation package (*29-32*). DFT electronic energy was computed using the PBE exchange function (*33*), a plane-wave basis set with a cutoff of 350 eV for expanding valence electrons wave-functions, and the PAW pseudo-potential (*34*) for core electrons. A k-point mesh of 2×2×1 was used, which was enough to converge absolute energy to within 0.02 eV. All calculations were performed assuming spin-paired configurations. Although the spin state might be important when Ni is present, performing spin-polarized calculations would make the CPU requirements prohibitive. Ni-Bi and Ni-Sn systems are nonmagnetic at the concentrations of Ni studied in this work, which suggests that there is no reason to suspect that Ni will have unpaired electrons in liquid Bi, Pb, or Sn. Spin-orbit coupling is not included in these calculations. For heavier elements such as Pt, spin-orbit coupling is important; however, the effect of spin-orbit coupling tends to destabilize Pt cluster. Therefore, it should not affect the qualitative results presented in this work.

Bader charges (*35*) were obtained by subtracting PAW explicit electrons from the integrated electron density inside the Bader volume, calculated with the algorithm developed by Henkelman (*36*). The reported Bader charges and projected density-of-states were computed by performing single-point calculations on configurations from AIMD trajectories with a cutoff of 400 eV and a k-point of 4×4×2. The simulation box was considered periodic in all directions, and dispersive van der Waal forces were incorporated using the pair-additive Grimme D3 method (*37*).

NVT AIMD simulations were performed with a target temperature of 900 K. The target temperature was achieved by Nosé-Hoover (*38-40*) method, which constructs an artificial Hamiltonian to sample equilibrium configurations at a constant temperature. The velocities for AIMD simulations were initialized from a Maxwell-Boltzmann distribution. Equations of motion were solved using the Verlet algorithm (*41*) with a time-step of 1 fs. The preparation of initial state of each run is discussed below.

Supplementary Text

Safety

The operation of molten-metal bubble columns requires safety protocols beyond what are typical in heterogeneous catalysis labs. High temperatures, heavy metal toxicity, and flammable gases present particular concerns. The Ni-Bi alloy described in this manuscript contains Bi, a heavy metal, and Ni, which has an exposure of 1 mg/m^3 per 8-hour work day regulated by OSHA. Bismuth has a vapor pressure of 1 kPa at 1050°C and its vapor may be carried

downstream. Bismuth toxicity is often mild but it can result in severe poisoning (*42*). If nickel salts are used in preparation of nickel metal, care should be taken in their handling as many are toxic. Nickel metal is also a known allergen, so care should be taken when handling solid nickel.

Quartz reaction vessels were used in many experiments because they are relatively inert; however, they are also fragile and cannot withstand stresses. Borosilicate glass should never be used or confused with quartz, and secondary containment of the liquid metal should always be used in case the reactor breaks -- a sand bath was placed beneath our bubble column. The flammability temperature and pressure limits of methane and hydrogen should be known and when operating outside of these limits, appropriate gas check valves and containment should be in place.

Single Pt, Ni, or Pd in molten metals (Sn, Bi, Pb)

We used single Pt, Ni or Pd atom in a film of Sn (or Bi or Pb) liquid consisting of 82 atoms. Since the whole system is periodically repeated, this corresponds to 1.2 mol % of Pt in Sn-liquid. The initial state (coordinates and velocities) was obtained by thermally equilibrating the system for 3 ps. The average Bader charges on Pt, Ni, and Pd atoms in various molten system is given in Table S1. The Bader charges on Pt during the first 5 ps of production run is shown in Figure 3b of the main text. Within the investigated time-scale, we find that the Bader charge on Pt fluctuates between –0.9 to and –1.12. A change in Bader charge by 0.2 electron is rather large. For example, the Bader charge difference between Mo in MoO_3 and Mo in MoO_2 is 0.5 electron, even though the formal charge differs by two electrons (*43*). Such a large fluctuations in Bader charge on Pt suggests that at different times a given Pt atom will have different reactivity.

Clusters of Pt, Ni, and Pd in molten metals (Sn, Bi, Pb)

To understand whether Pt in molten alloy forms clusters or is present as isolated atoms, we investigated the behavior of one Pt_2 cluster placed in molten Sn. This corresponds to ~2.4 mol % Pt in Sn liquid. The initial state of Pt_2 cluster in Sn liquid was obtained as follows: (a) A Pt_2 cluster was cut from Pt solid. (b) A cavity was created in molten Sn and Pt_2 cluster was placed in the cavity. (c) AIMD was performed for 3 ps by keeping Pt-Pt distance in Pt_2 fixed and letting Sn relax around it. The final coordinates and velocities from these equilibration runs were used to perform production AIMD run with no fixed atoms. As discussed in the main text (see Figure 3d), Pt_2 breaks into Pt atoms in less than 9 ps and the Bader charge on each Pt is approximately –1. This is remarkable because in the gas phase the Pt^{2-} and Pt^{4-} ions are bound by more than 0.5 eV, according to DFT calculations with the HSE06 functional. We further investigated the behavior of a Pt_8 cluster in molten Sn liquid which corresponds to ~ 9 mol% of Pt in molten Sn. This concentration is near Pt saturation in molten Sn, at 900 K. To generate an initial guess for Pt_8 clusters in molten Sn we proceeded as follows: we performed AIMD of gas-phase Pt_8 cluster for 10 ps at 900 K. We extracted the Pt_8 configuration that had the lowest energy and placed it in a cavity inside molten Sn. We then fixed the positions of Pt and performed AIMD for another 3 ps, allowing the Sn atoms to relax. The final coordinates and velocities were used as an initial guess for the production run. We also performed AIMD with a Pt_8 cluster that had the same coordination as eight Pt atoms in solid Pt. All these calculations

give the same qualitative result: the Pt_8 disintegrates surprisingly fast. The evolution of the radius of gyration of Pt_8 is shown in Fig. S10 and clearly the "size" of the cluster expands very rapidly. Fig. S11 shows that in 7 picoseconds each of the eight Pt atoms has a charge close to –1. A bar graph of the mean charges (the mean is an average of the charge of the same atom over time) on each Pt atom is shown in Fig. S9.

Similar results were obtained for Ni_8 cluster in molten bismuth. The qualitative behavior is the same in all systems investigated here.

Removal of carbon from the reactor

We propose two methods of carbon removal. The first method is to "skim" the carbon from the surface mechanically. This method is commonly employed in removal of slag material from melts in metallurgical processes. In the second method, the carbon produced in a Ni-Bi column was light enough that significant quantities could be entrained in the gas flow and carried downstream. This could be used in a large-scale reactor to remove the carbon and optimized by increasing the superficial velocity at the surface through geometric design, introducing hydrogen at a high flow rate, or introducing an inert gas at a high flow rate to carry the carbon downstream to a cyclone, bag filter, or other solid-gas separation method.

Estimating the reactor size for a 200 kiloton per year H_2 plant

In multi-phase reactions, large-scale reactors are difficult to model reliably and, without scale-up data, all results are subject to considerable uncertainty. Nevertheless, using a few defensible assumptions, we can make some progress in estimating larger-scale reactor sizes based on lab data. A more precise determination of reactor size requires scale-up experiments. In principle, methane pyrolysis occurs both inside the bubble and at the gas-liquid contact area (bubble surface). Experiments using similar bubbles in inert molten salts show that the gas phase reaction (inside the bubbles) is negligible. Based on this observation we assume that all methane reacts at the gas-liquid interface of the bubbles, with a rate proportional to the surface area.

We obtained kinetic data in a differential reactor with known gas-liquid area. This kinetic information and the measured conversion were used to calculate the surface area in a 1-meter-long bubble column constructed in our lab (see Figure 3a). The results were used to extrapolate to an 800-kta CH_4 pyrolysis plant as a first-pass estimate of reactor size.

Using the activation energy, pre-exponential, and methane-pressure dependences obtained in the differential bubble column for the NiBi alloy, a rate law was developed in terms of the gas-surface interface area in the catalytic melt. The rate r (in moles per cm^2-s) is

$$r = k[CH_4] = A e^{\frac{-E_A}{RT}} [CH_4] \quad (1)$$

where k is the rate constant in mL cm^{-2} s^{-1} and $[CH_4]$ is methane concentration in mol/L.

The reaction rate r was observed to be first-order in methane pressure (Figure 3b). This rate law was then used to derive an expression for the methane conversion, X, as a function of surface area, SA. It is common in reactor engineering models to use a steady-state flow reactor mass balance where the change in the molar flowrate of methane, dF_{CH_4}, is

$$dF_{CH_4} = -F_{CH_4,0} dX = -r\, dSA \quad (2)$$

where $dF_{CH_4,0}$ is the inlet methane molar flowrate. Eq. 2 is the mass balance for a differential element having the area dSA. Using the rate expression above in this mass balance gives

$$F_{CH_4,0}\,dX = k[CH_4]\,dSA \tag{3}$$

and the methane concentration will vary with methane conversion in the bubble as

$$[CH_4] = [CH_4]_0 \frac{(1-X)}{(1+\varepsilon X)} \frac{P}{P_0} \tag{4}$$

where ε, reflecting the change in moles, is in this case equal to the initial mole fraction $y_{CH_4,0}$ of methane in the feed. The total pressure P used for the 1.1-meter column includes the hydrostatic pressure determined by using the measured density of the liquid. The pressure drop was neglected for the 200-kta unit because at an entrance pressure P_0 of 10 bar, the pressure drop is less significant. The relationship between the reactor conversion and surface area is then

$$\frac{dX}{dSA} = \frac{k[CH_4]}{F_{CH_4,0}} = k\frac{[CH_4]_0}{F_{CH_4,0}} \frac{(1-X)}{(1+\varepsilon X)} \frac{P}{P_0} \tag{5}$$

which can be integrated to give the conversion as a function of surface area encountered by the gas (which is proportional to reactor height):

$$\int_0^X \frac{(1+\varepsilon X)}{(1-X)} dX = k\frac{[CH_4]_0}{F_{CH_4,0}} \int_0^{SA} \frac{P}{P_0} dSA \tag{6}$$

The relationship is compared to the data from our 1-meter bubble column at 1040°C in Figure 3a.

The same calculation method (integrating over reactor gas-liquid surface area) is used as an estimate for the reactor size required for pyrolysis of 800 million kilograms per year (800 kilotons per year = 800 kta) of CH_4 to make 200 kilotons per year (200 kta) of H_2. In both cases, the mass transport lengths are less than 10 mm within reaction times of several seconds at 10 atm or less, at approximately 1065°C. We can safely neglect mass transfer limits to the reaction on the two-phase surface. The reactor is then assumed to have no transport limitations and to be dependent on the gas-liquid surface area, not the bulk liquid or gas. The system is also assumed to have separable hydrogen and carbon which do not react ($k_{rev} \sim 0$): the reaction between hydrogen and dissolved carbon was not observed; the rate when the melt was saturated with H_2 was the same as the initial rate (Figures S2 and S3), despite the fact that the dissolved carbon concentration went from 0% to saturation.

For the 200-kta hydrogen production unit, using the experimental data and the expression above, the estimated surface area required for 90% conversion is 9.7×10^8 cm^2. Assuming the bubble column has a typical commercial reactor "hold-up" (ratio of gas volume in bubbles to total reactor volume) of 25%, and that the average bubble radius is 0.5 cm (surface to volume ratio, $0.5/\pi$), the reactor volume is approximately, 6.2×10^8 $cm^3 = 620$ m^3.

Summary of notation

F_{CH_4} = molar flow rate of methane [moles of CH_4 per minute]

$F_{CH_4,0}$ = inlet molar flow rate of methane into the reactor [moles of CH_4 per minute]

SA = surface area of catalytic surface reaction [cm^2]

X = conversion of methane

$\varepsilon = y_{CH_4,0}\left(\frac{2}{1}-1\right)$ to account for the stoichiometric change in number of moles

$y_{CH_4,0}$ = initial molar fraction of methane

P = total pressure [atm]

P_0 = total pressure at reactor inlet [atm]

$[CH_4]_0$ = initial methane concentration at reactor inlet [mol/L]

Values used for 200-kta hydrogen plant size estimate

E_A = activation energy = 208 kJ/mol

pre-exponential A = $e^{15.88}$ mL cm^{-2} s^{-1}

$k = 60\ A\ e^{-E_A/(8.314\times10^{-3}T)}$ (from Arrhenius plots [cm^3 / (min*cm^2)])

$F_{CH_4,0}$ = 95,130 moles CH_4 / min

$y_{CH_4,0}$ = 1

P_0 = 10 atm

T = 1065 + 273 K

$[CH_4]_0 = (P_0/(R\ T))\ y_{CH_4,0}$

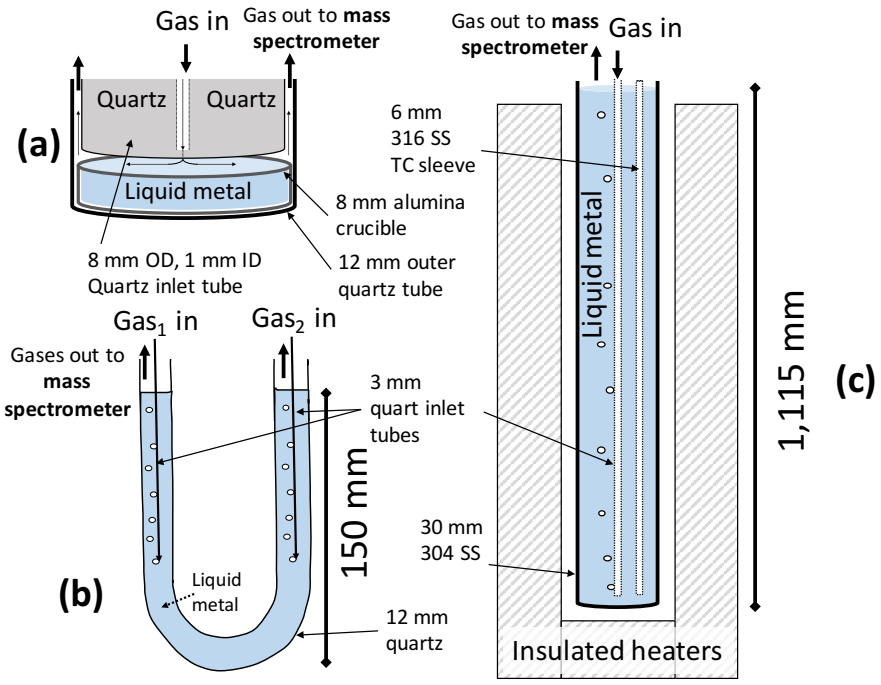

Fig. S1. (a) Schematic of the screening reactor used to determine liquid metal activity. 38.5 mm^2 of liquid metal was used and filled the alumina crucible. (b) Schematic of quartz bubble column reactor in U-tube geometry. (c) Schematic of 1.1-m stainless steel bubble column reactor. All reactors were in thermally insulated electric heaters.

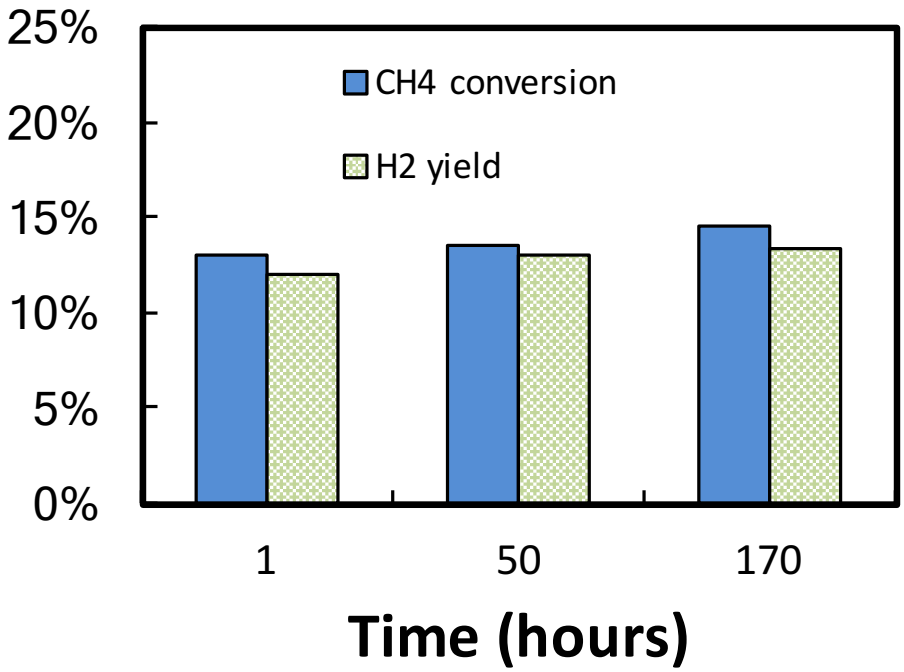

Fig. S2. Methane conversion and hydrogen yield in reactor described in Fig. S1 at 1000°C with inlet tube introduced 80 mm below the surface with 9 sccm methane and 1 sccm argon.

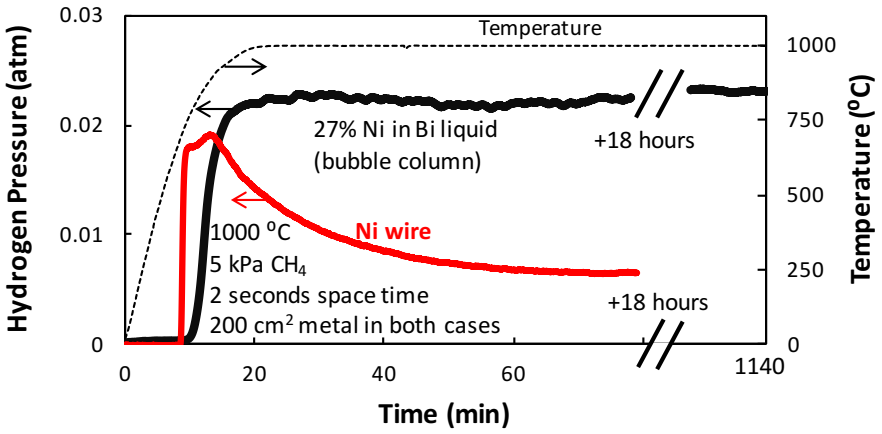

Fig. S3. Hydrogen from methane pyrolysis as a function of time on stream for solid Ni wire and for a bubble column of 27 % mole Ni-Bi liquid. The estimated surface area is 200 cm^2 of solid Ni and 200 cm^2 of liquid surface area in the bubbles. The temperature is 1000°C and the residence time is 2 seconds. At time 0, the reactor is heated and the variation of the temperature with time is indicated by the dotted line (the temperature is recorded on the right side).

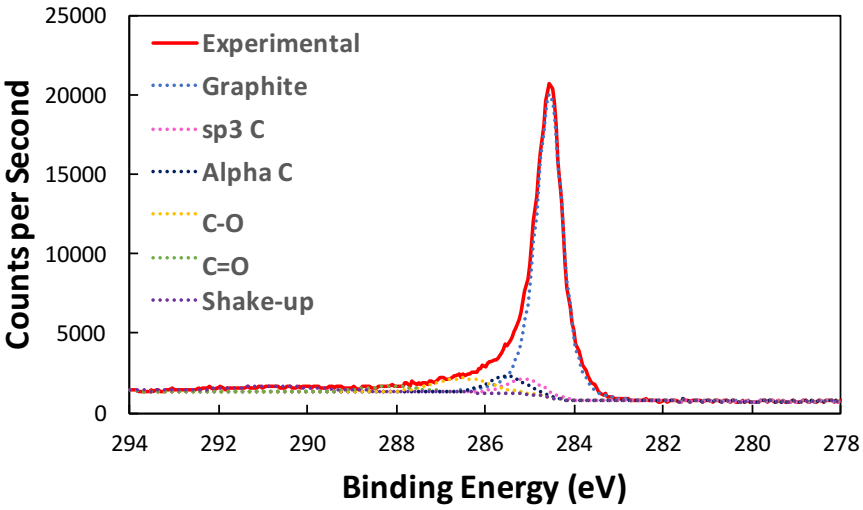

Fig. S4. XPS of carbon collected at the surface of molten 27 mol % Ni-Bi after 7 days at 1050°C in pure methane flowing at 10 sccm. The spectrum indicates that most carbon is graphite. The sample was conductive to the point that it did not require charge neutralization and the sharp peak is naturally centered at 285.4 eV with full-width-half-max below 0.7 eV, suggesting the sample is primarily sp2 carbon. The other carbons present had full-width-half-max above 1 eV. Note: a carbide would be 1.5V lower, and the contribution of each carbon type to the experimental spectra is fit in the dotted lines.

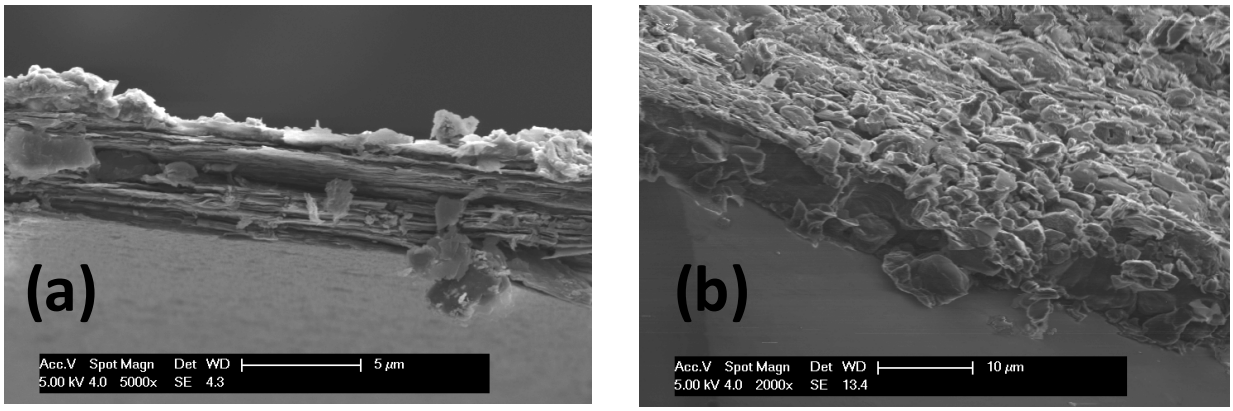

Fig. S5. SEM images of carbon deposited at the interface of the melt with the wall of the reactor: (a) after 30 hours, (b) after 1 week.

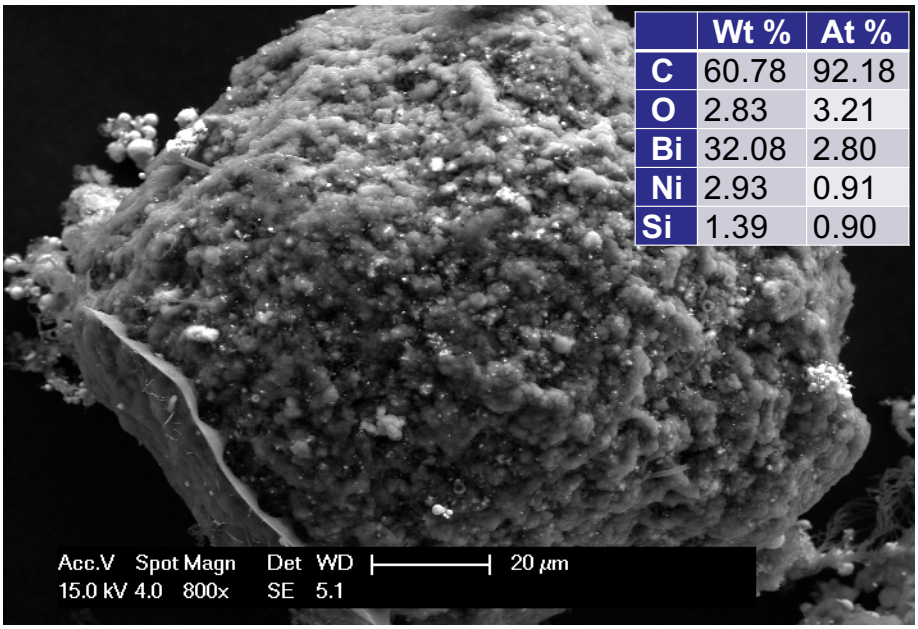

Fig. S6. SEM image of carbon removed from the surface after cooling the melt. The carbon was produced on the surface of a 27 mol % NiBi melt after 20 hours of 5 kPa methane and 95 kPa argon bubbling through a bubble column at a temperature of 1000°C and a residence time of 2 seconds. The insert shows EDS data taken from a square encompassing most of the particle in the image**.**

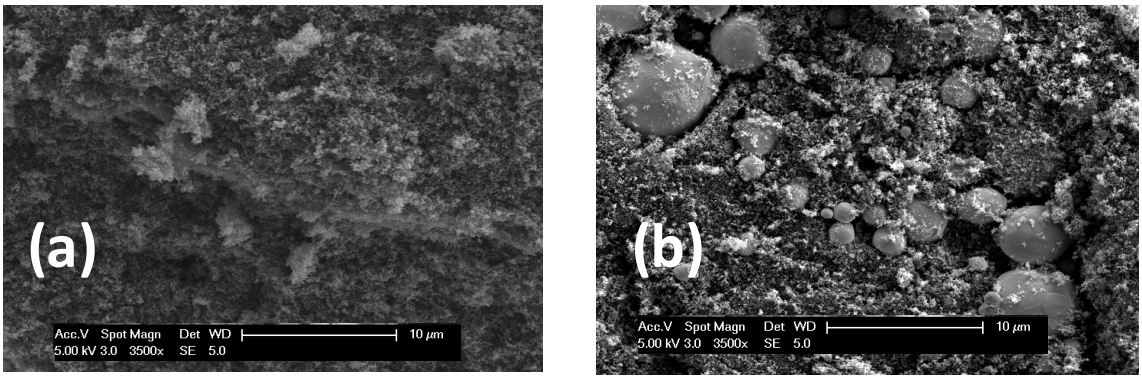

Fig. S7. SEM images of carbon black (a) as purchased and (b) after sitting on a 150-mm bubble column of 27 mol % Ni in Bi in 5 sccm argon at 1050°C for 20 hours

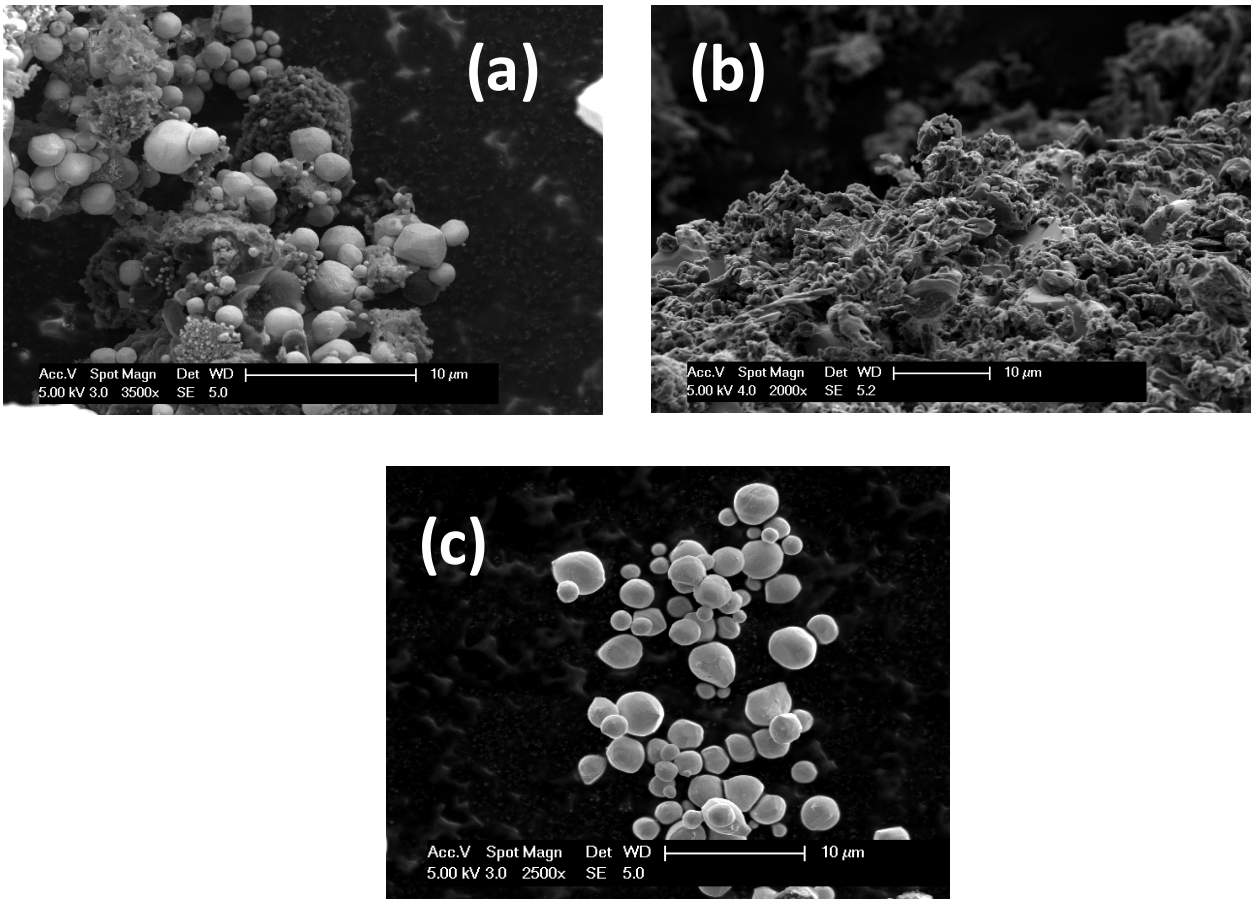

Fig. S8. SEM images: (a) carbon formed at the surface of a 27% NiBi bubble column, (b) carbon formed by placing the carbon from (a) at the bottom of a 6-inch column of liquid 27% NiBi at 1000°C rapidly cooled to room temperature, (c) bismuth evaporated and then condensed, in the absence of any carbon source, from a 27% NiBi bubble column at 1050°C.

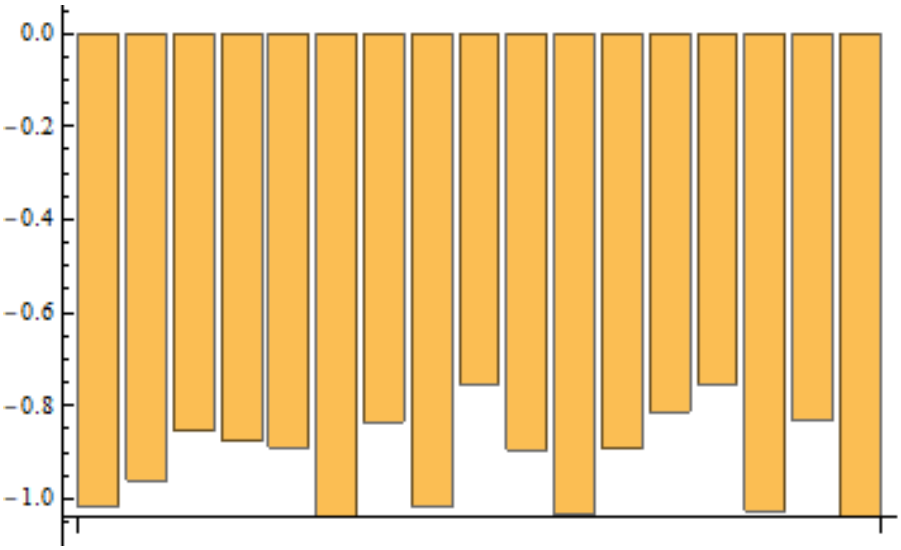

Fig. S9. Bar chart showing the average (over a full molecular dynamics run) charge on each of the 17 Pt atoms dissolved in 82 atoms of Sn. The average of this charge is –0.91 electron. Even at this high concentration the Pt atoms do not form clusters.

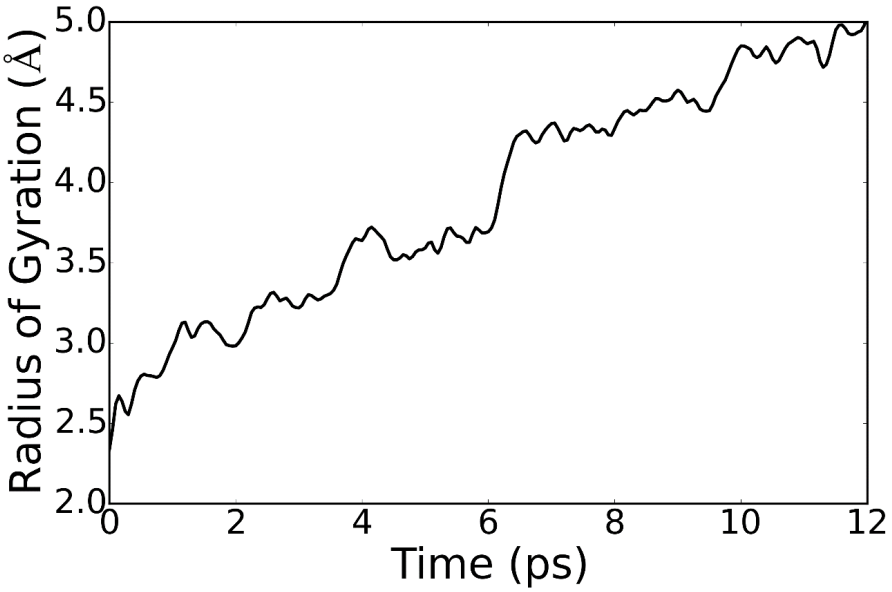

Fig. S10. The time evolution of the radius of a Pt_8 cluster during a MD run in a melt containing 45 Sn atoms, at 627°C

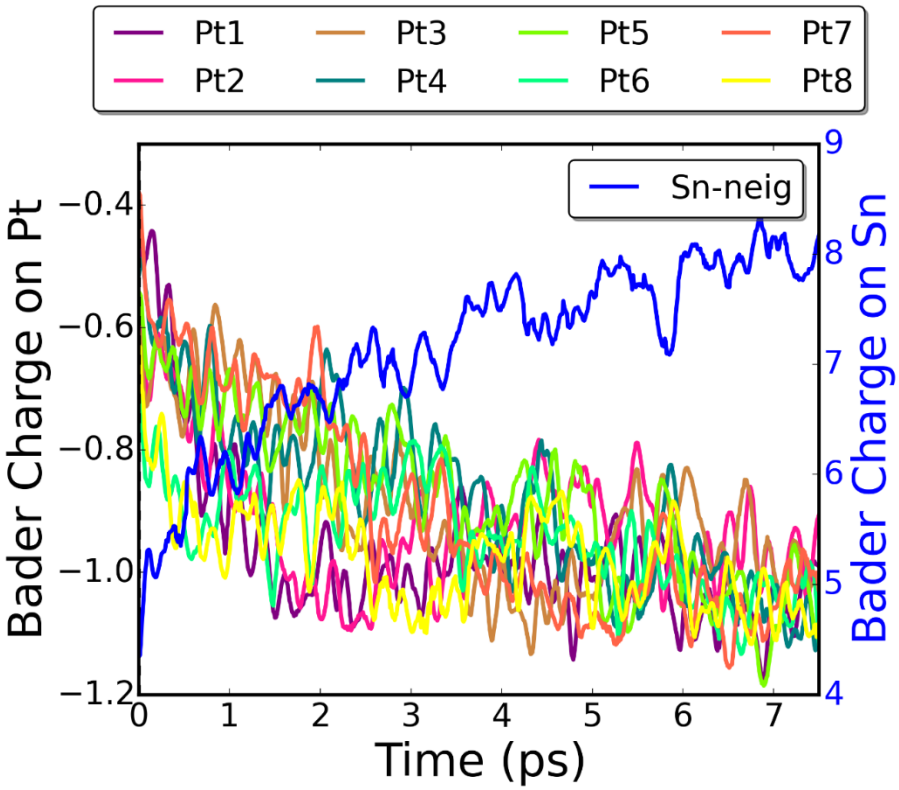

Fig. S11. Bader charges on Pt atoms in Sn liquid during an AIMD run. The initial state is a Pt_8 cluster solvated in Sn liquid, which dissociates into single solvated Pt atoms as the time progresses. Also shown are the sum of Bader charges on the neighboring Sn atoms. The cut-off distance for neighboring Sn is taken to be 3.5 Å.

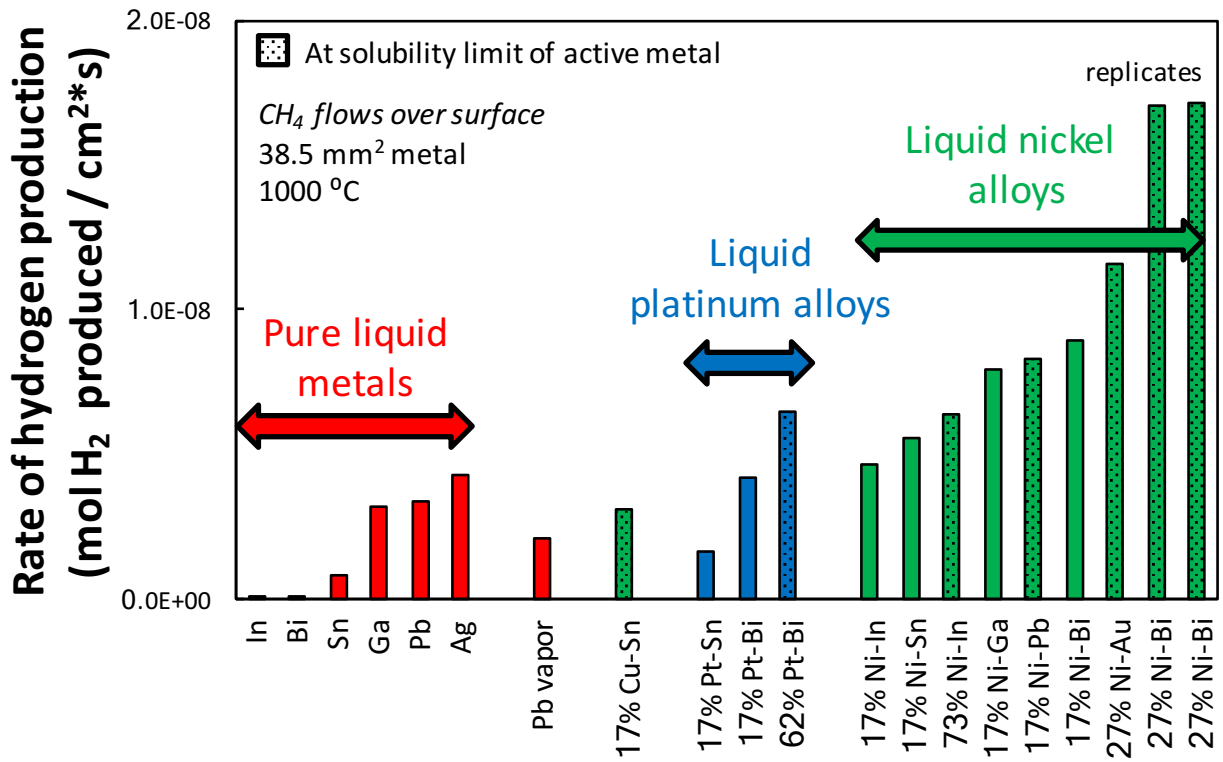

Fig. S12. Graphical comparison of activity reported in Table 1 for methane pyrolysis at 1000 °C, over 38.5 mm^2 of molten metal. The same reactor volume was used in all cases, including for Pb vapor. All compositions are molar percent.

Atom	Bader Charge		
	Sn-liquid	**Bi-liquid**	**Pb-liquid**
Ni	-0.44 ± 0.009	-0.28 ± 0.006	-0.30 ± 0.004
Pd	-0.66 ± 0.007	-0.45 ± 0.004	-0.53 ± 0.005
Pt	-1.01 ± 0.007	-0.82 ± 0.004	-0.87 ± 0.005

Table S1. Average Bader charges of active metals (Pt, Ni and Pd) in molten "inert" metals (Sn, Bi, Pb). The averages are computed for 5 ps with data collected at every 100 fs.

Caption for Movie S1

A movie showing changes in projected density of states of the Pt atom during an AIMD run. EF is the Fermi energy. Also shown are the projected density of states for Sn atoms which are nearest-neighbors to the Pt atom and the projected density of states of all the Sn atoms. The cut-off distance of neighboring Sn atoms from the Pt atom is 3.5 Å. In the middle of the plot we show partial charge density (green) for the orbital which has the maximum contribution to the Pt-like orbitals for an isovalue of 0.05 e/ $Å^3$. The corresponding energy level is shown by dotted green line on the density of states plot. The Sn atoms are shown in gray and the boundaries of simulation box in dark blue.

Caption for Movie S2

A movie showing changes in Bader charges and Bader volume of Pt_2 cluster dissociating in Sn liquid. In the bottom panel, we show the evolution of the Bader charges on the two Pt atoms and neighboring Sn atoms during an AIMD run. The dotted red line corresponds to the time in the MD run for which Bader volumes are shown in the top panel. Sn atoms are gray and the boundaries of the simulation box is dark blue. In the top left panel we show Bader volume on Pt atoms (green and orange). In top middle panel we show increase and in the top right panel we show decrease in the Bader charge density compared to that of the two Pt atoms in gas-phase separated by the same distance as in liquid Sn. All Bader volumes are shown for an isovalue of 0.05 e/ $Å^3$.